

# Smaller Sensitivity of Precipitation to Surface Temperature under Massive Atmospheres

Junyan Xiong<sup>1</sup>, Jun Yang<sup>1</sup>, and Jiachen Liu<sup>1</sup>

<sup>1</sup>Laboratory for Climate and Ocean-Atmosphere Studies, Department of Atmospheric and Oceanic Sciences, School of Physics, Peking University, Beijing 100871, China

## Key Points:

- Numerical simulations show that under a given surface temperature, the precipitation is weaker if the air mass is larger.
- The increasing rate of global-mean precipitation with surface temperature under a larger air mass is also smaller.
- The combined effect of air mass on Rayleigh scattering, multiple scattering, pressure broadening, and lapse rate is the mechanism.

arXiv:2209.02294v1 [astro-ph.EP] 6 Sep 2022

---

Corresponding author: Jun Yang, [junyang@pku.edu.cn](mailto:junyang@pku.edu.cn)

**Abstract**

Precipitation and its response to forcings is an important aspect of planetary climate system. In this study, we examine the strength of precipitation in the experiments with different atmospheric masses and their response to surface warming, using three global atmospheric general circulation models (GCMs) and one regional cloud-resolving model (CRM). We find that precipitation is weaker when atmospheric mass is larger for a given surface temperature. Furthermore, the increasing rate of precipitation with increasing surface temperature under a larger atmospheric mass is smaller than that under a smaller atmospheric mass. These behaviors can be understood based on atmospheric or surface energy balance. Atmospheric mass influences Rayleigh scattering, multiple scattering in the atmosphere, pressure broadening, lapse rate, and thereby precipitation strength. These results have important implications on the climate and habitability of early Earth, early Mars, and exoplanets with oceans.

**Plain Language Summary**

Precipitation is one of the key variables of the planetary climate system. Many factors can influence the strength of precipitation, such as solar flux, land-sea distribution, greenhouse gases, and aerosols. In this study, we show that another factor, atmospheric mass, can also strongly influence precipitation. The strength of precipitation increases with increasing surface temperature but decreases with increasing atmospheric mass. Furthermore, the increasing rate of precipitation with surface temperature becomes smaller under a larger atmospheric mass. These results have important implications for the climate evolution of early Earth, early Mars, and extra-solar rocky planets, which may have higher or lower air mass than that of modern Earth.

**1 Introduction**

Precipitation is an important aspect of the climate system. Precipitation and its related latent heat release are one of the main driving factors of the atmospheric circulation on Earth (Holton & Hakim, 2013). The spatial pattern of precipitation (as well as evaporation) and its variability influence the distribution of vegetation over the land (Lotsch et al., 2003) and the surface salinity and density over the ocean (Huang, 1993). The seawater density further influences the global oceanic overturning circulation that transports energy from the tropical region to higher latitudes (Vallis, 2017). Furthermore, the strength of precipitation and its related runoff strongly affect the rate of carbonate-silicate weathering process, which determines atmospheric CO<sub>2</sub> concentration in geological timescales and then in turn influences the surface and air temperatures and precipitation (Walker et al., 1981; Nagy, 2018). The strength and spatial pattern of precipitation can be influenced by many factors, such as solar radiation, greenhouse gases, land-sea configuration, and aerosols. In this study, we emphasize another factor, atmospheric mass, which can strongly influence the strength of precipitation.

The atmospheric mass of Earth evolves with time. Before the first Great Oxidation Event in  $\sim 2.4$  billion years ago (Gya), atmospheric O<sub>2</sub> concentration ( $pO_2$ ) was negligible, and before the Neoproterozoic Oxidation Event in  $\sim 0.6$  Gya, it was about 10% or less of the present level (Holland, 2006). For early Earth, Marty et al. (2013), Som et al. (2016), and Avicé et al. (2018) showed that the surface pressure was likely less than the present level, and the lower limit is unconstrained but maybe smaller than 0.5 bar, but global nitrogen budget suggests that N<sub>2</sub> partial pressure might be  $\geq 3$  bar (Goldblatt et al., 2009; Johnson & Goldblatt, 2015; Mallik et al., 2018). For Mars, its surface pressure might be 1–2 bar in its early stage, but now it is only  $\sim 0.006$  bar (Lammer & Bauer, 1991). For Venus, its surface pressure is close to 93 bar, mainly composed of CO<sub>2</sub> (Basilevsky & Head, 2003). Titan has a surface pressure of 1.45 bar (Niemann et al., 2005), but since the surface gravity of Titan is  $1.35 \text{ m s}^{-2}$  ( $\sim 0.14$  of Earth's), its air mass per unit area is  $\sim 10.5$  times Earth's value. For

planets beyond the solar system (or called exoplanets), their atmospheric masses, as well as compositions, can be quite different from those in the solar system (Turbet et al., 2018; Madhusudhan, 2019).

Previous studies have shown that atmospheric mass has strong effects on planetary surface temperature (Goldblatt et al., 2009; Charnay et al., 2013; Le Hir et al., 2014; Kopparapu et al., 2014; Wolf & Toon, 2014; Keles et al., 2018; Xiong & Yang, 2020; Y. Zhang & Yang, 2020; Paradise et al., 2021) and on atmospheric circulation (e.g., Kaspi & Showman, 2015; Chemke et al., 2016; Chemke & Kaspi, 2017; Guendelman & Kaspi, 2019; Komacek & Abbot, 2019; Xiong et al., 2020). Here, we focus on another climatic variable, surface precipitation. Using numerical simulations, Poulsen et al. (2015) found that the strength of precipitation increases when  $p\text{O}_2$  is reduced. They proposed that the mechanism is related to the reduction of Rayleigh scattering of air molecules under a lower  $p\text{O}_2$  and thereby the increase of surface shortwave radiation. In this study, we extend their work by considering a much wider range of atmospheric mass. Furthermore, we explore the dependence of the increasing rate of precipitation with surface warming on atmospheric mass. For the mechanism, we find that atmospheric mass can influence not only shortwave radiation but also longwave radiation, both of which can influence the strength of precipitation, and the change of longwave radiation can significantly influence the increasing rate of global-mean precipitation with surface temperature.

## 2 Model descriptions and experimental designs

Our numerical simulations are mainly carried out using the Community Atmospheric Model version 3.0 (CAM3, Collins et al., 2004, 2006) and the Exoplanet Community Atmospheric Model (ExoCAM). CAM3 is a widely used model developed by the National Center for Atmospheric Research (NCAR). The radiative transfer scheme in CAM3 is based on Ramanathan and Downey (1986) and Briegleb (1992). The deep convection parameterization scheme is developed by G. J. Zhang and McFarlane (1995). Clouds are treated as three types: marine stratus, convective clouds, and layered clouds. ExoCAM is developed based on CAM version 4.0 (CAM4). ExoCAM calculates radiative transfer with correlated- $k$  method based on the database of HITRAN 2004 (Wolf & Toon, 2013, 2015; Wolf et al., 2022). The CAM3 simulations have 26 vertical levels and the horizontal resolution is  $2.8^\circ \times 2.8^\circ$ . In the ExoCAM simulations, we use 40 vertical levels with a horizontal resolution of  $4^\circ \times 5^\circ$ . Eight main groups of experiments are designed, as listed in rows 2 to 9 of Table 1. For each group, we change the partial pressure of  $\text{N}_2$  to test five different atmospheric masses, 0.5, 1, 5, 10, and 30 bar. In all the experiments, the gravity is  $9.8 \text{ m s}^{-2}$ .

In group A, we use CAM3 to perform the simulations, and surface temperature ( $T_s$ ) is fixed with a meridional distribution of  $T_s(\theta) = T_{ref} + \Delta T \times (1 - \sin^2(\theta))$ , where  $T_{ref}$  is a reference temperature, which is varying from 275 K to 295 K with a 5-K interval,  $\Delta T$  is the equator–pole temperature difference, and  $\theta$  is latitude (Neale & Hoskins, 2000; Medeiros et al., 2008). Two different values of  $\Delta T$  are tested, 20 and 50 K. The solar constant is  $1365 \text{ W m}^{-2}$ . The radiatively active gases include  $\text{CO}_2$  (0.36 mbar),  $\text{CH}_4$  ( $0.8 \mu\text{bar}$ ),  $\text{N}_2\text{O}$  ( $0.27 \mu\text{bar}$ ), and  $\text{O}_3$  (pre-industrial condition, see Dütsch, 1978). The surface is ocean everywhere with no continent; this is called an aqua-planet.

In group B, the experiments are the same as in group A, except that the atmosphere is coupled to a slab ocean, rather than with fixed- $T_s$ . The ocean depth is 50 m everywhere and no ocean heat transport is included. To obtain an appropriate temperature range, different  $\text{CO}_2$  concentrations are performed for each surface pressure: for 0.5 bar, the  $\text{CO}_2$  concentrations are 0.36, 0.72, 1.44, 2.88, and 5.76 mbar; for 1.0 bar, the  $\text{CO}_2$  concentrations are 0.18, 0.36, 0.72, 1.44, and 2.88 mbar; for 5.0 bar, the  $\text{CO}_2$  concentrations are 0.09, 0.18, 0.36, 0.72, and 1.44 mbar; and they are 0.045, 0.09, 0.18, 0.36, 0.72 mbar for 10.0 and 30.0 bar. The solar constant is fixed,  $1365 \text{ W m}^{-2}$ .

**Table 1.** Models and Experimental Designs

Groups	Model	Surface	Land–Sea	Surface Pressure	Descriptions
A	CAM3	Fixed- $T_s$	Aqua-planet	0.5, 1, 5, 10, 30 bar	Fixed $S_0$ and $CO_2$
B	CAM3	Slab ocean	Aqua-planet	0.5, 1, 5, 10, 30 bar	Fixed $S_0$ , varied $CO_2$
C	CAM3	Slab ocean	Aqua-planet	0.5, 1, 5, 10, 30 bar	Varied $S_0$ , fixed $CO_2$
D	CAM3	Slab ocean	Aqua-planet	0.5, 1, 5, 10, 30 bar	Varied $S_0$ and $CO_2$
E	CAM3	Slab ocean	Modern continents	0.5, 1, 5, 10, 30 bar	Fixed $S_0$ , varied $CO_2$
F	CAM3	Slab ocean	Modern continents	0.5, 1, 5, 10, 30 bar	Varied $S_0$ , fixed $CO_2$
G	CAM3	Slab ocean	Modern continents	0.5, 1, 5, 10, 30 bar	Varied $S_0$ and $CO_2$
H	ExoCAM	Fixed- $T_s$	Aqua-planet	0.5, 1, 5, 10, 30 bar	Fixed $S_0$ and $CO_2$
	ExoRT	Fixed- $T_s$	Sea surface	0.5, 1, 5, 10, 30 bar	1-D radiative transfer model
Sens1	CAM3	Fixed- $T_s$	Aqua-planet	10 bar	Weakened pressure broadening
Sens2	CAM3	Slab ocean	Aqua-planet	10 bar	Change solar radiation
Sens3	PlaSim	Slab ocean	Modern continents	0.5, 1, 5, 10 bar	Paradise et al. (2021)
Sens4	SAM	Slab ocean	Sea surface	0.5 and 1 bar	Small-domain, cloud-resolving

In group C, the experiments are similar to group B, but the partial pressure of  $CO_2$  is fixed to 0.36 mbar, and the solar constant is varied: for 0.5 and 1.0 bar, the solar constant is 1330, 1365, 1400, 1430, and 1460  $W m^{-2}$ ; for 5.0 bar, the solar constants are 1290, 1320, 1340, 1365, and 1400  $W m^{-2}$ ; for 10.0 bar, the solar constants are 1270, 1300, 1330, 1365, and 1400  $W m^{-2}$ ; for 30.0 bar, the solar constants are 1250, 1275, 1300, 1330, and 1365  $W m^{-2}$ .

In group D, the experimental design is similar to group B, but both  $CO_2$  concentration and solar constant are varied. Five different  $CO_2$  concentrations are performed: 0.18, 0.36, 0.72, 1.44, and 2.88 mbar, for all the five surface pressures. We have also changed the insolation to keep  $T_s$  in an appropriate range. For the 0.5 bar surface pressure, the solar constant is 1400  $W m^{-2}$ , and 1365  $W m^{-2}$  for 1 bar, 1320  $W m^{-2}$  for 5 bar, 1300  $W m^{-2}$  for 10 bar, and 1250  $W m^{-2}$  for 30 bar.

Group E is the same as group B, group F is the same as group C, and group G is the same as group D, except that modern Earth’s land-sea distribution is used, rather than an aqua-planet mode. These three groups are performed to test the effect of land–sea configuration.

In group H, the experiments are the same as group A but use the model ExoCAM. Comparing group H with group A, we can know whether our conclusion is robust under different radiative transfer schemes. Briefly, the greenhouse effect of water vapor in ExoCAM is stronger, and shortwave absorption by water vapor in ExoCAM is also stronger than in CAM3. For more details, please see J. Yang, Leconte, et al. (2016), Kopparapu et al. (2017), and Wolf et al. (2022).

To clarify the underlying mechanism, we have also done a series of 1-D radiative transfer calculations with the Exoplanet radiative transfer model (ExoRT, Wolf et al., 2017) and several groups of GCM sensitivity experiments (see Table 1). Using ExoRT, five different surface pressures are considered: 0.5, 1, 5, 10, and 30 bar. Under each surface pressure,  $T_s$  is varied from 285 to 305 K with 5-K intervals. The temperature structures are moist adiabatic profiles, with a 150-K isothermal stratosphere. In the troposphere, the atmosphere is set to be saturated. In the stratosphere, the specific humidity is set to be equal to the value at

the top of the troposphere. For the details and results of the GCM sensitivity experiments, please see section 3.3 below.

In the GCM experiments of fixed- $T_s$ , the model takes less than 10 model years to reach equilibrium. We run the experiments for 15 years. Data of the last 5 model years are used to analyze below. In the GCM experiments of slab ocean, the model takes about 30 model years to reach equilibrium. Each experiment was run for at least 40 years, and the last 10 years are analyzed. In all the 3-D simulations, the vertical profiles of temperature, water vapor, clouds, and other variables are actively coupled to radiation, advection, and convection processes, regardless if the fixed- $T_s$  or slab ocean setup was used. After reaching equilibrium, annual-mean net atmospheric energy imbalance is within  $\pm 0.5 \text{ W m}^{-2}$  in all the experiments. Meanwhile, time series of surface temperature and precipitation fields were analyzed and they have also reached equilibrium.

### 3 Results

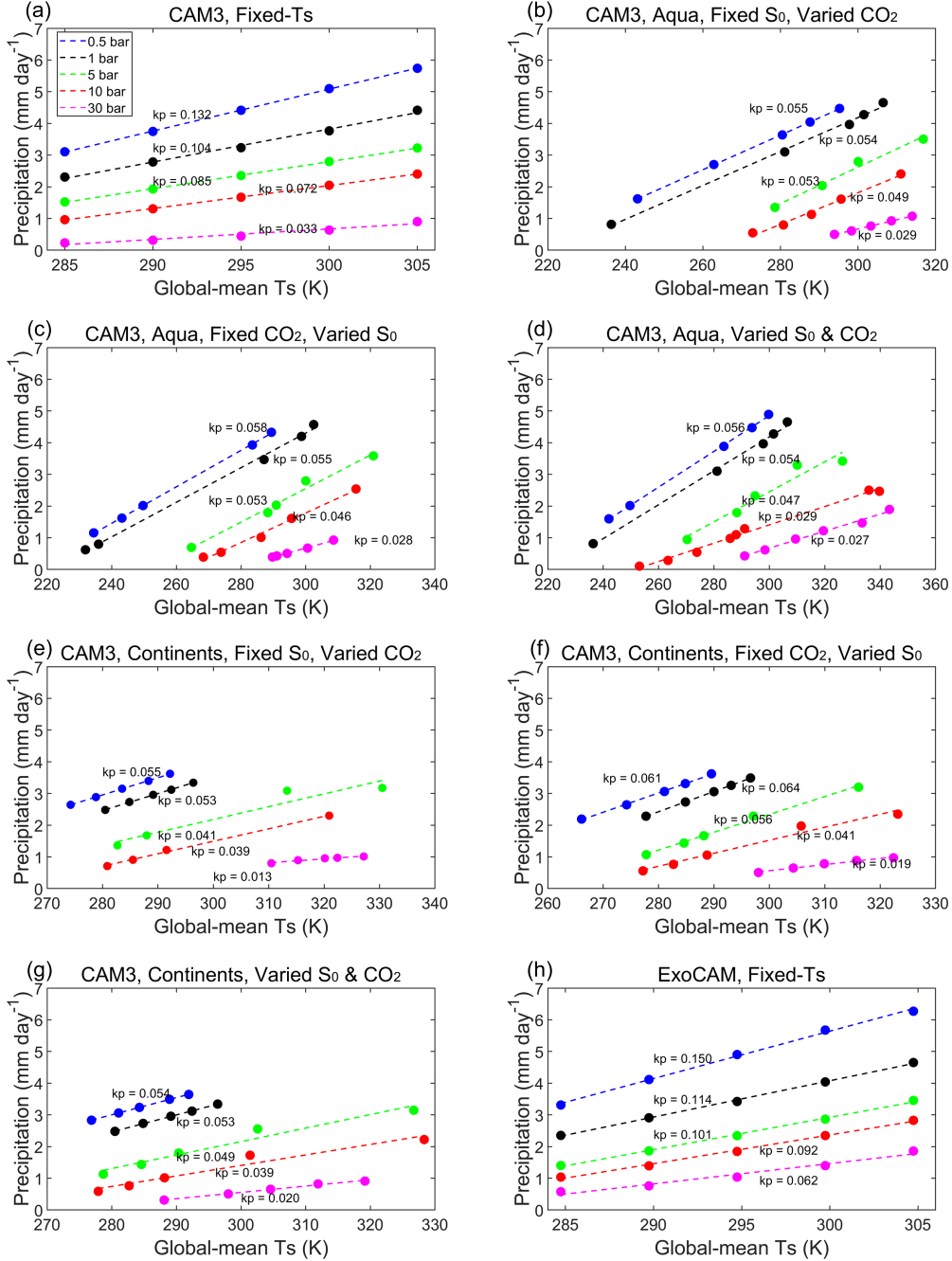
#### 3.1 Dependence of precipitation- $T_s$ relationship on atmospheric mass

Figure 1 shows annual- and global-mean precipitation as a function of global-mean  $T_s$  in all eight groups of experiments. Due to different surface boundary conditions (fixed- $T_s$  or coupled to a slab ocean, and with or without continents), different surface temperature ranges, different external forcings (varied stellar radiation,  $\text{CO}_2$  concentration, or both), and different models (CAM3 and ExoCAM), the absolute strengths of precipitation (including both rainfall and snowfall) are different between the groups. But, all these eight groups show three clear trends: 1) the precipitation is a nearly linear increasing function of  $T_s$ ; 2) under a given global-mean  $T_s$ , the precipitation is weaker when the surface pressure is higher; 3) the slope of precipitation- $T_s$  strongly depends on the value of surface pressure, and it decreases under a higher surface pressure. The first trend is not new and it has been found in many previous studies of global warming such as Trenberth and Shea (2005), Lambert and Webb (2008), and J. Yang, Peltier, and Hu (2016). So, in the following, we will focus on the second and third trends.

Figures S1–S8 show the spatial patterns of annual-mean precipitation in the eight groups of experiments. There are two precipitation-concentrated regions, one in the deep tropics where there is strong intertropical convergence and one in middle latitudes where there is strong baroclinic instability. The three trends listed above can be found in both these two regions. This implies that the trends do not depend on the detailed dynamical processes (convergence, instability, monsoon, or storm track) or the type of convection (deep, shallow, or mixed). There should be some unified mechanism that determines the behavior of the mean precipitation.

#### 3.2 Mechanism

In the analyses of precipitation change under global warming, many studies have found that atmospheric or surface energy balance is a good approach, which can quantitatively estimate the change of precipitation under different conditions (e.g., Pierrehumbert, 2002; Allen & Ingram, 2002; O’Gorman et al., 2012; Showman et al., 2013; Pendergrass & Hartmann, 2014; Jeevanjee & Romps, 2018). A diagram of the atmospheric energy budget is shown in Figure 2a. The air receives shortwave radiation from the star, reflects a part of the shortwave radiation back to space, obtains longwave radiation, sensible heat, and latent heat from the surface, and meanwhile emits longwave radiation to space and surface. In the long-term and global mean, the amount of latent heat that acts to heat the atmosphere is equal to the amount of atmospheric net energy loss (i.e., atmospheric net longwave emission – atmospheric shortwave absorption – sensible heat). Meanwhile, the value of net latent heat release is equal to the amount of surface precipitation ( $P$ ) multiplied by the specific



**Figure 1.** Annual- and global-mean precipitation as a function of global-mean  $T_s$  in the eight groups of experiments. (a) group A in which  $T_s$  is fixed, the model is CAM3, and it is in an aqua-planet mode (see also Figure S9). (b) group B, same as (a) but the surface is actively coupled to a 50 m slab ocean,  $CO_2$  concentration is varied but the solar constant is fixed ( $1365 \text{ W m}^{-2}$ ). (c) group C, same as (b) but  $CO_2$  concentration is fixed to 0.36 mbar and the solar constant is varied. (d) group D, same as (b) but both  $CO_2$  concentration and solar constant are varied. (e)-(g) are same as (b)-(d) but with modern Earth's land-sea distribution. (h) group H, same as (a) but using the model ExoCAM. The dashed lines are the linear regressions. The slope of each regression line is listed near the line with units of  $\text{mm day}^{-1} \text{ K}^{-1}$ . Two main conclusions: 1) the precipitation is weaker under a higher air mass for a given  $T_s$ , and 2) the precipitation- $T_s$  slope is flatter under a higher air mass, although the absolute values differ significantly among the different groups.

heat of water vaporization ( $L$ ) and the density of liquid water ( $\rho_w$ ), written as:

$$L\rho_w P = LH = LW^a - SW^a - SH \quad (1)$$

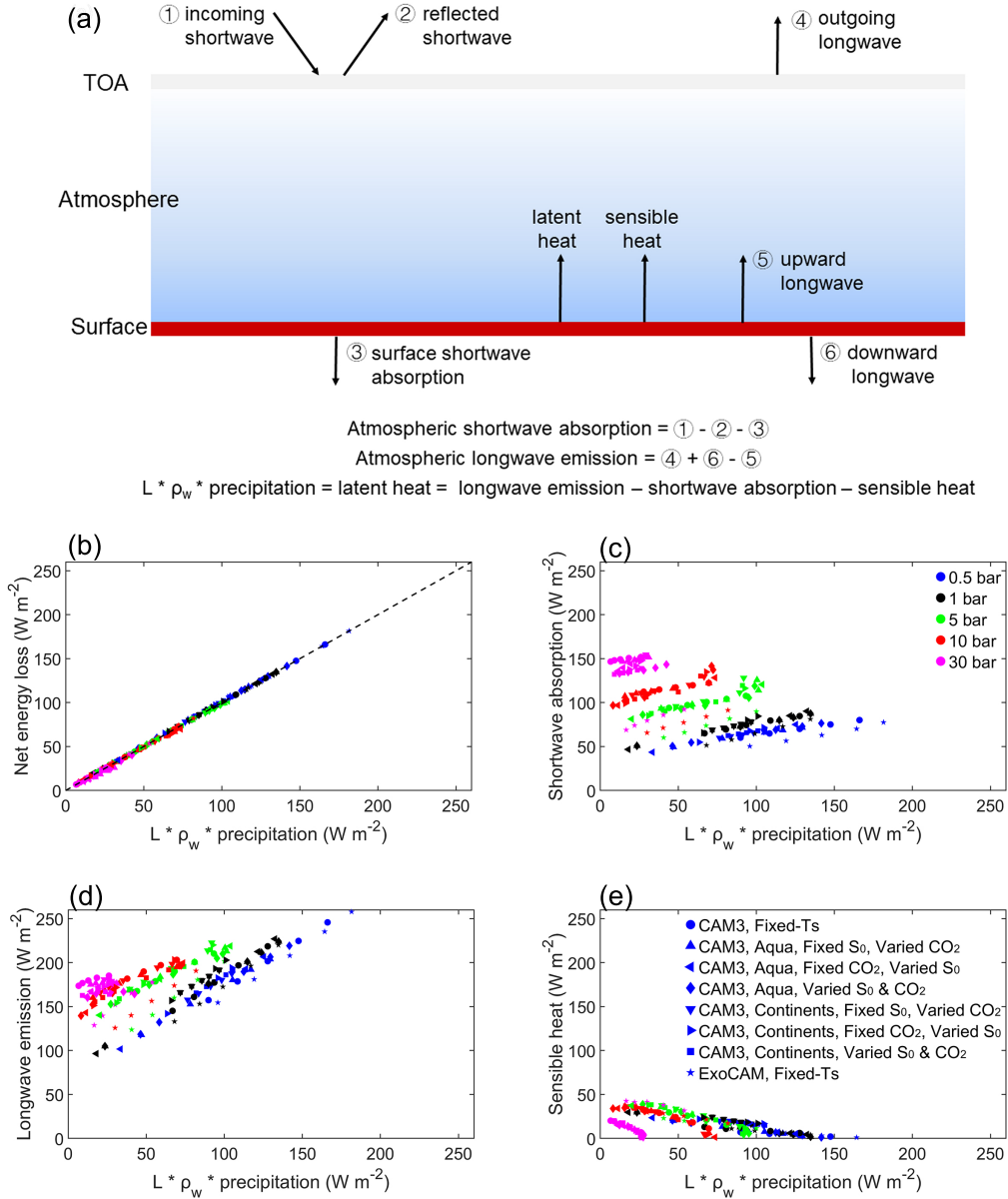
where  $LH$  is surface latent heat flux,  $LW^a$  is atmospheric net longwave emission,  $SW^a$  is atmospheric shortwave absorption, and  $SH$  is surface sensible heat flux. All these terms are global-mean values, so horizontal heat and water transports are not explicitly included.

Figure 2b shows the relationship between the atmospheric net energy loss and the precipitation rate multiplied by  $L$  and  $\rho_w$ . All the experiments of the eight groups fall in the 1-to-1 diagonal line; this confirms that the above atmospheric energy budget is correct and also implies that the atmosphere has already reached equilibrium in all the experiments. In the fixed- $T_s$  experiments, the surface is not energy-balanced, but the net energy gain or loss at the surface is equal to that at the top of the atmosphere (TOA, figures not shown). Figures 2c, 2d, & 2e show the atmospheric shortwave absorption, atmospheric net longwave emission, and surface sensible heat flux, respectively. It can be seen that the atmosphere net longwave emission dominates, and the sensible heat flux is the smallest but not negligible. This is similar to that on modern Earth, for which the three values are  $\approx 80$ , 188, and  $20 \text{ W m}^{-2}$ , respectively (Hartmann, 2015). In the CAM3 experiment with modern continents,  $\text{CO}_2$  concentration, and solar flux (in the group F), the global-mean surface temperature is 289 K and the three values are 74, 180, and  $20 \text{ W m}^{-2}$ , respectively.

Why does the precipitation rate become smaller under a larger atmospheric mass even under the same global-mean  $T_s$ ? The answer is shown in Figure 3. There are two reasons. One is that the atmospheric net longwave emission decreases and the other one is that the atmospheric shortwave absorption mainly by water vapor in near-infrared wavelengths increases, as air mass is increased.

The former, the change of the atmospheric net longwave emission, is because the atmospheric greenhouse effect becomes stronger with increasing air pressure, which in turn, is mainly because of the effect of pressure broadening and the change of vertical temperature profile. As the surface pressure increases under a given surface temperature, upward longwave emission to space decreases (Figures 3c & S10), downward longwave radiation to the surface increases (Figure 3e), and the change of the former is larger than that of the latter, so that the atmospheric net longwave emission decreases (Figure 3h). These trends can also be found in 1-D off-line radiative transfer calculations, as shown in Figures S11, S12 & S13. In longwave wavelengths, the effect of increased pressure broadening is qualitatively equivalent to adding more  $\text{CO}_2$  to the atmosphere. Both of them act to increase the atmospheric greenhouse effect by trapping more thermal radiation from the surface and then re-emitting back to the surface, i.e., the thermal transmissivity of the atmosphere decreases (see Text S1, Figure S14 in Supporting Information, and Li et al., 1997). Meanwhile, a higher air mass increases the atmospheric heat capacity and thereby makes the lapse rate larger (i.e., closer to dry adiabat, Figure S11, S15 & S16, see also such as Nakajima et al. (1992), Goldblatt et al. (2009) and Xiong et al. (2020)). This leads to a stronger atmospheric greenhouse effect and less atmospheric longwave emission to space, which leads to weaker precipitation according to equation (1).

The latter, the increase of atmospheric shortwave absorption, is because increasing air mass enhances multiple scattering in the atmosphere, which means that the shortwave absorption path of water vapor becomes longer (Figures 3g & 2c). Meanwhile, when air mass is increased, more shortwave energy is reflected back to space due to enhanced Rayleigh scattering (Figures 3a & S17), so less shortwave energy reaches the surface (Figure 3b); based on this, Poulsen et al. (2015) suggested that surface evaporation (and precipitation) should become smaller, because the global-mean evaporation should be equal to surface shortwave absorption minus net surface longwave emission and surface sensible heat flux (the framework of surface energy budget). These results are consistent with off-line 1-D radiative-transfer calculations (Figure S17, see also Lacis and Oinas (1991), Paynter and Ramaswamy (2011), and Goldblatt (2016)). Moreover, from Figures 3a, 3b, & 3g, one could



**Figure 2.** (a) Schematic diagram of how global-mean precipitation is determined by energy budget in the system. In global-mean, latent heat release (associated with precipitation) is equal to atmospheric net energy loss, which is equal to the combination of atmospheric longwave emission, atmospheric shortwave absorption, and surface sensible heat flux. (b) Atmospheric net energy loss vs precipitation; (c) atmospheric shortwave absorption vs precipitation; (d) atmospheric net longwave emission vs precipitation; and (e) surface sensible heat flux vs precipitation. The global-mean precipitation has been multiplied by  $L \rho_w$ , where  $L$  is the specific heat of water vaporization, and  $\rho_w$  is the density of liquid water. The definition of the directions of the different variables in panels (b)-(e) follows panel (a). This figure shows that the precipitation strength is constrained by net energy loss in the atmosphere, regardless of the surface type, fixed- $T_s$  or coupled to a slab ocean.



find that in these experiments the changes of the shortwave flux at the TOA and at the surface are about 5–10 times that of the changes of the absorbed shortwave flux in the atmosphere; the former is the component of TOA or surface energy budget, the latter is the component of atmospheric energy budget, and there is no contradiction between them.

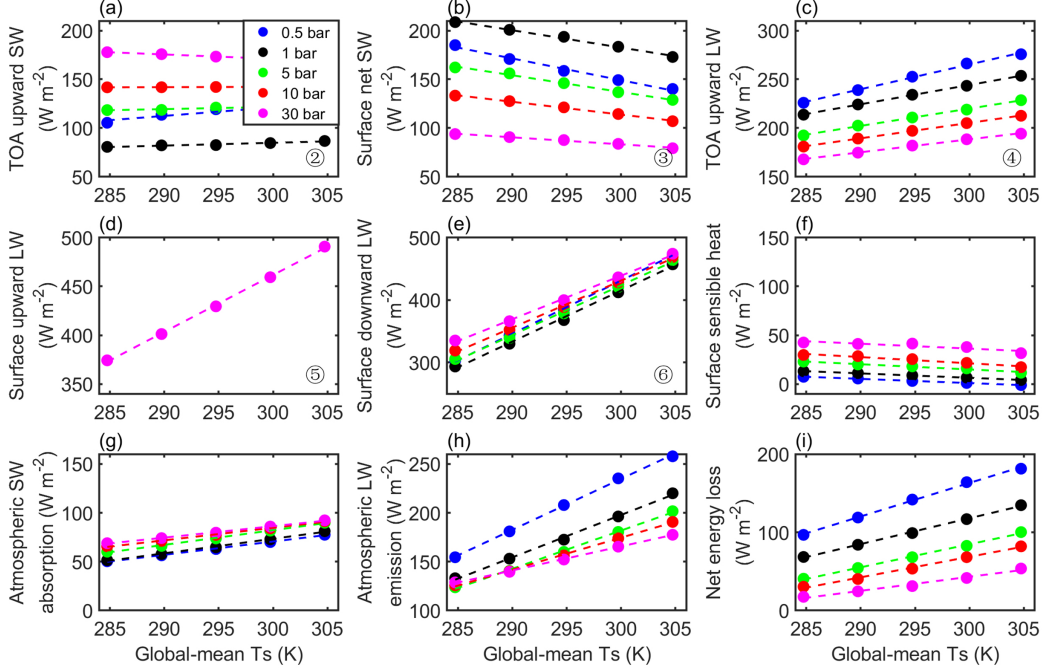


**Figure 3.** Global-mean atmospheric energy budget as a function of  $T_s$  in the group H experiments. (a) Upward shortwave (SW) flux at the top of the atmosphere (TOA), (b) net shortwave flux at the surface, (c) upward longwave (LW) flux at the TOA, (d) upward longwave flux at the surface, (e) downward longwave flux at the surface, (f) surface sensible heat flux, (g) atmospheric shortwave absorption, (h) atmospheric longwave emission, and (i) atmospheric net energy loss. The definition of the directions of the different variables follows Figure 2a. In panel (d), the values for different surface pressures are the same because the surface temperatures are the same (specified). The numbers of ② to ⑥ in panels (a)–(e) are corresponding to those in Figure 2a. Precipitation strength is constrained by atmospheric net energy loss (see equation (1)).

Why does the precipitation– $T_s$  slope become smaller under a larger atmospheric mass? The answer is also shown in Figure 3, in particular, the upward longwave emission at the TOA or called outgoing longwave radiation (OLR) shown in Figure 3c. OLR is contributed from two parts: one is the portion of the emission from the surface which is transmitted by the entire atmosphere, and the other one is from the atmosphere itself (Pierrehumbert, 2010). OLR is a nearly linear increasing function of  $T_s$  over a wide range of temperatures, unless the surface is too cold (such as below 190 K) or too hot (such as above 320 K). This is because of the competition between the increased surface thermal emission with temperature and the narrowing of spectral window regions ( $\approx 8\text{--}12\ \mu\text{m}$ ) related to the increase in atmospheric water vapor concentration (Koll & Cronin, 2018; Y. Zhang et al., 2020). The slope of the OLR– $T_s$  relation depends on the surface temperature and the average transmissivity of the atmosphere (equation [3] and Figure 4 in Koll & Cronin, 2018). In our experiments, the transmissivity is lower under a higher atmospheric mass (Figure S14), so the OLR– $T_s$  slope becomes smaller. Another reason for the decrease of the OLR– $T_s$  slope is that the increase of air temperature of the upper troposphere under a higher surface pressure is smaller than that

under a lower surface pressure, for the same  $T_s$  change (as shown in Figure S11, S15 & S16). This also makes the sensitivity of OLR to  $T_s$  become smaller (Figure 3c & S10). Again, the underlying mechanism relates to that the temperature profile is steeper under a larger air mass (see Text S2 in Supporting Information).

The decreasing trend of the OLR– $T_s$  slope with increasing atmospheric mass was also found in previous clear-sky radiative transfer calculations, such as shown in Figure 5b of Goldblatt et al. (2013), Figure 1a of Kopparapu et al. (2014), and Figure 1a in Y. Zhang and Yang (2020). Note that this trend occurs only when the atmosphere is below the runaway greenhouse limit. In the runaway greenhouse state, the atmosphere becomes optically thick in all thermal wavelengths due to the continuum absorption of water vapor and thereby OLR nearly does not depend on  $T_s$  (Koll & Cronin, 2018). In other words, for very optically-thick conditions, the upper troposphere becomes the primary emission layer and subsequently OLR is decoupled from the surface.

Figures S13a & S18 show that for a given surface temperature, the amount of vertically-integrated water vapor is lower under a higher air mass (because the atmospheric temperature profile is closer to dry adiabat), but the corresponding value of OLR is smaller rather than greater in both 3-D GCMs and 1-D radiative transfer models (Figures 3c, S10, & S13c). This is counter-intuitive as it is well known that water vapor has a strong greenhouse effect and in general a lower water vapor content should be corresponding to a greater OLR. But, the pressure broadening effect of the changed air mass is strong and the lapse rate is larger (closer to dry adiabat) for a higher air mass, which acts to trap more thermal radiation and decrease the value of OLR.

The third term on the right side of equation (1) is surface sensible heat flux. In the model, sensible heat flux is calculated by  $\rho c_p C_D W (\theta_s - \theta_a)$ , where  $\rho$  is the near-surface air density,  $c_p$  is the specific heat capacity of air,  $C_D$  is stability-dependent turbulent exchange coefficient,  $W$  is surface wind speed, and  $\theta_s$  and  $\theta_a$  are the potential temperatures of surface and near-surface air, respectively. Surface wind speed decreases with increased atmospheric mass, due to the decreases of horizontal temperature gradients under massive atmospheres, which in turn is related to the increase of meridional energy transport under a higher air mass (Figure S19; for more details, please see Chemke et al. (2016) and Chemke and Kaspi (2017)). Meanwhile, the temperature difference ( $\theta_s - \theta_a$ ) also decreases under a higher air mass. The near-surface air density, however, increases significantly (figures not shown). As a result, higher air mass leads to larger sensible heat flux, as shown in Figure 3f. This also implies that the precipitation should become weaker under a higher atmospheric mass, based on the energy balance constraint in equation (1). But, the change of the sensible heat– $T_s$  slope under different atmospheric masses is very small (Figure 3f), so that the precipitation– $T_s$  slope is not influenced by the changes of the sensible heat flux.

### 3.3 Sensitivity experiments and results

In order to further confirm the mechanisms, we perform four sensitivity groups of experiments, as listed in rows 11 to 14 of Table 1. As addressed in section 3.2, pressure broadening is one of the important factors, which influence longwave radiative transfer and thereby the precipitation strength. To more clearly examine this, we add one group of experiments within which the surface pressure is 10 bar but the effect of pressure broadening is set to that of 1 bar. When the pressure broadening is weakened, the slope of the precipitation– $T_s$  relationship increases from 0.072 to 0.089 mm day<sup>-1</sup> K<sup>-1</sup> (Figure 4a). This confirms that pressure broadening has an effect of reducing the precipitation– $T_s$  slope.

Also addressed in section 3.2, shortwave radiation can influence the strength of precipitation but nearly does not influence the precipitation– $T_s$  slope. To further confirm this, we add one group of experiments within which the solar constant is changed from 1300 to 1092 W m<sup>-2</sup>. The precipitation– $T_s$  slope almost stays unchanged (Figure 4b). This confirms that

shortwave radiation is not the key factor that influences the precipitation– $T_s$  slope but it does influence  $T_s$  and the absolute value of precipitation.

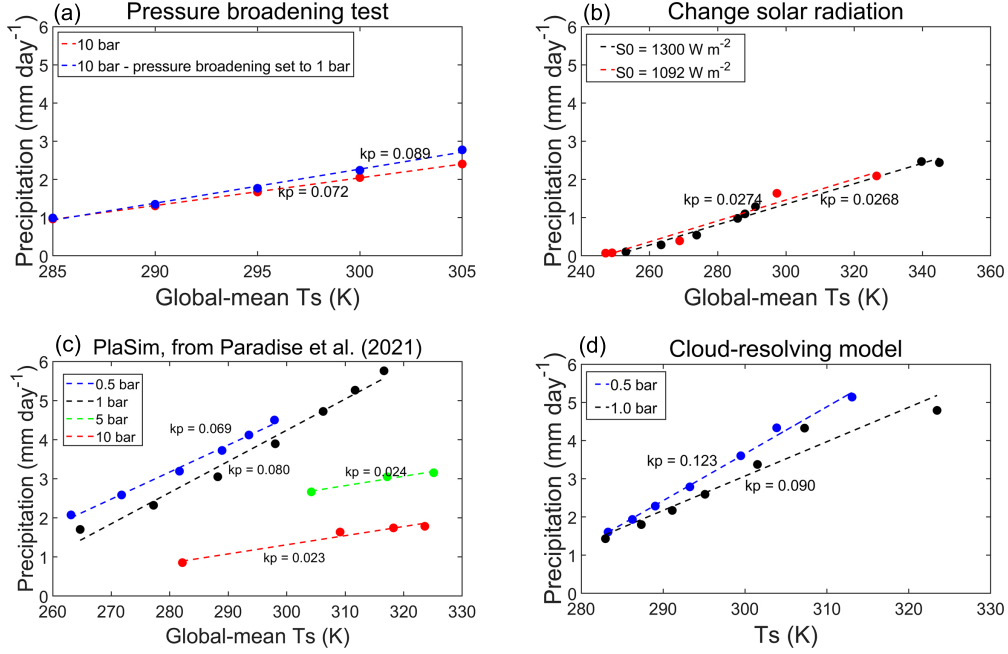


**Figure 4.** Results of the sensitivity experiments. (a) The run of 10.0 bar surface pressure (red line) and the sensitivity run of 10.0 bar with pressure broadening set to 1 bar (blue line), using CAM3 with fixed- $T_s$ ; (b) the runs of changing solar constant from 1300 to 1092  $\text{W m}^{-2}$ , using CAM3 coupled to a 50-m slab ocean; (c) the results of another GCM PlaSim with data from Paradise et al. (2021), and (d) the results of cloud-resolving simulations without convection parameterization, using SAM coupled to a slab ocean. The lines are for linear regressions. These sensitivity experiments confirm the two conclusions found in Figure 1.

Besides CAM3 and ExoCAM, we find that our main results can also be verified in another GCM, PlaSim. The results of PlaSim are shown in Figure 4c, and the data was downloaded from the Borealis repository (Paradise et al., 2021). Paradise et al. (2021) employed the model to examine the effects of varying  $\text{N}_2$  partial pressure on surface temperature, sea ice coverage, clouds, and atmospheric circulation. PlaSim is coupled to a 50-m slab ocean; the convection scheme and radiative transfer scheme of PlaSim are relatively simpler than CAM3 and ExoCAM; the model resolution,  $5.625^\circ$  in latitude and  $5.625^\circ$  in longitude, is lower than CAM3 and ExoCAM; and modern Earth’s land-ocean configuration was used in their simulations. Although the radiative transfer module, convection parameterization, and cloud and precipitation schemes in PlaSim are different from CAM3 or ExoCAM, the basic effects of varying air mass on Rayleigh scattering, pressure broadening, and lapse rate are included. So, it is not a surprise to view the same conclusions in PlaSim.

In CAM3, ExoCAM, and PlaSim, convection and clouds are parameterized. The model resolutions are not fine enough to resolve convection processes. In the final sensitivity group, we use a cloud-resolving model, the System of Atmospheric Modeling (SAM, Khairoutdinov & Randall, 2003). SAM uses a non-hydrostatic dynamic core and employs the radiative transfer module of RRTM (a rapid and accurate radiative transfer model, Mlawer et al., 1997) that is similar to that used in ExoCAM, but ExoCAM can more accurately simulate extremely hot and wet climates such as runaway greenhouse (Wolf et al., 2022). We employ

a domain of  $96 \text{ km} \times 96 \text{ km}$ , and the horizontal resolution is  $1 \text{ km} \times 1 \text{ km}$ . The time step is 10 s. Two surface pressures are tested, 0.5 and 1 bar. Each SAM experiment runs for 2500 model days. The outputs of the last 100 days are analyzed. Under 0.5 bar, the precipitation– $T_s$  slope is  $0.123 \text{ mm day}^{-1} \text{ K}^{-1}$ , but it decreases to  $0.090 \text{ mm day}^{-1} \text{ K}^{-1}$  when surface pressure is 1 bar (Figure 4d). These results indicate that our conclusions do not rely on the convection/cloud schemes.

#### 4 Conclusions and Discussions

In this study, we have explored the dependence of global-mean precipitation on atmospheric mass and its sensitivity to  $T_s$  change. First, the strength of precipitation decreases with air mass under a given  $T_s$ . Second, the slope of the precipitation– $T_s$  relationship becomes flatter under a higher air mass. These trends can be understood based on atmospheric or surface energy balance budget. The first result is contributed by the combined effect of increased Rayleigh scattering, enhanced atmospheric shortwave absorption, weakened net atmospheric longwave emission, and increased surface sensible heat flux as air mass is larger. The latter is due to that longwave atmospheric transmissivity becomes smaller and meanwhile the lapse rate becomes steeper when air mass is increased.

This study emphasizes a new factor, atmospheric mass, which can influence the sensitivity of global-mean precipitation to  $T_s$ . Over geological time scales or on other rocky planets, the atmospheric masses can be significantly different from modern Earth. Different atmospheric masses influence the response of precipitation to  $T_s$  and therefore the timescale of the carbonate–silicate weathering cycle. This coupled process can further influence global climate, its evolution, and planetary habitability. In particular, these results suggest that precipitation is very weak on planets having massive atmospheres, which can strongly limit planetary habitability.

In this research, we explain the response of precipitation to air mass through energy balance budget. But, atmospheric dynamics may offer another way to understand the results. For example, when atmospheric mass increases, the strengths of the meridional circulation and convection would decrease (Chemke et al., 2016; Chemke & Kaspi, 2017). The extra-tropical eddies also become weaker because of less mean eddy kinetic energy per unit mass (Chemke & Kaspi, 2017). The advantage of the approach we used here is that energy balance budget is more quantitative and easier to analyze.

Figures 1 and 4 show that there are large quantitative differences in the precipitation strength and the precipitation– $T_s$  slope between aqua-planets and planets with modern Earth’s continents. Also, there are significantly quantitative differences between the three models, CAM3, ExoCAM, and PlaSim. It is important to know what exact mechanisms/processes cause the differences in the future. These results also suggest that in studying precipitation under different climate states, one model is not enough and a hierarchy of models or multiple models are required.

In this study, we focus on the variable of precipitation. But, other related variables of the climate system, such as cloud fraction, cloud water path, and water vapor concentration (Figure S18), are also influenced by atmospheric mass. These variables can strongly influence observational atmospheric characteristics such as transmission, emission, and reflection spectra. Moreover, in our experiments, the land water storage has also changed, which can influence the types of surface vegetation if it existed on exoplanets. All these are left for future work.

More experiments in the future are required to examine whether the conclusions are applicable to other planets, such as planets with different background gases (such as  $\text{H}_2$ , He,  $\text{O}_2$ , CO, or  $\text{CO}_2$ ), planets having different gravities, different stellar spectra, and tidally locked planets with different rotation rates or spin-orbit resonances. In our experiments, air mass, the number of molecules, and surface air pressure are changed, but both planetary

gravity ( $9.8 \text{ ms}^{-2}$ ) and background atmospheric molecular weight ( $28 \text{ g mole}^{-1}$ ,  $\text{N}_2$ ) are fixed. The separated effects of these different factors are not explicitly addressed in this article. For example, Rayleigh and Mie scatterings depend on the number of molecules and the inherent properties of molecules (such as  $\text{N}_2$  versus  $\text{CO}_2$ ), the strength of pressure broadening depends on air mass and planetary gravity, and the molecular weight compared to  $\text{H}_2\text{O}$  can strongly influence the strength of buoyancy for convection. Previous studies had examined the effect of varying planetary gravity on radiation transfer, surface temperature, and atmospheric dynamics (such as Pierrehumbert, 2010; Kaspi & Showman, 2015; Kilic et al., 2017; H. Yang et al., 2019; H. Yang & Yang, 2019; Thomson & Vallis, 2019), but no work has explored its effect on surface precipitation. Moreover, another important process related to precipitation strength is shortwave absorption, which is strongly influenced by water vapor concentration, clouds, and stellar spectrum. Water vapor and clouds have greater absorption coefficients in near-infrared wavelengths. If the star has a redder spectrum, more stellar energy would be absorbed by the atmosphere (rather than by the surface), therefore the atmosphere would be more stable (e.g., Eager et al., 2020) and convection and precipitation would be weaker. All these should be further examined in future studies.

## Open Research

The simulation data is available at: <https://doi.org/10.5281/zenodo.7011993>. The CAM3 code is available at: [www.cesm.ucar.edu/models/atm-cam/](http://www.cesm.ucar.edu/models/atm-cam/). The CESM code is available at: [www.cesm.ucar.edu/models/cesm1.2/](http://www.cesm.ucar.edu/models/cesm1.2/). The ExoCAM and ExoRT are available at: <https://github.com/storyofthewolf/ExoCAM>. The SAM code is available at: <http://rossby.msrc.sunysb.edu/~marat/SAM.html>. The PlaSim simulation data can download from from the Borealis repository: <https://doi.org/10.5683/SP2/LOFVCV> (Paradise et al., 2021).

## Acknowledgments

Jun Yang is supported by the National Natural Science Foundation of China (NSFC) under grants 42075046 and 42161144011. Our simulations use about  $3.0 \times 10^5$  core-hours in total, and this is corresponding to  $\text{CO}_2$  emission of about  $4.8 \times 10^2$  kg, if assume the power per core is 3.7 W and the average carbon emission intensity is around 0.7 kg per kWh.

## References

- Allen, M. R., & Ingram, W. J. (2002). Constraints on future changes in climate and the hydrologic cycle. *Nature*, *419*(6903), 228–232. doi: 10.1038/nature01092
- Avice, G., Marty, B., Burgess, R., Hofmann, A., Philippot, P., Zahnle, K., & Zakharov, D. (2018). Evolution of atmospheric xenon and other noble gases inferred from Archean to Paleoproterozoic rocks. *Geochimica et Cosmochimica Acta*, *232*, 82–100. doi: 10.1016/j.gca.2018.04.018
- Basilevsky, A. T., & Head, J. W. (2003). The surface of Venus. *Reports on Progress in Physics*, *66*(10), 1699. doi: 10.1088/0034-4885/66/10/R04
- Briegleb, B. P. (1992). Delta-Eddington approximation for solar radiation in the NCAR Community Climate Model. *Journal of Geophysical Research: Atmospheres*, *97*(D7), 7603–7612. doi: 10.1029/92JD00291
- Charnay, B., Forget, F., Wordsworth, R., Leconte, J., Millour, E., Codron, F., & Spiga, A. (2013). Exploring the faint young Sun problem and the possible climates of the Archean Earth with a 3-D GCM. *Journal of Geophysical Research: Atmospheres*, *118*(18), 10–414. doi: 10.1002/jgrd.50808
- Chemke, R., & Kaspi, Y. (2017). Dynamics of massive atmospheres. *The Astrophysical Journal*, *845*(1), 1. doi: 10.3847/1538-4357/aa7742
- Chemke, R., Kaspi, Y., & Halevy, I. (2016). The thermodynamic effect of atmospheric mass on early Earth's temperature. *Geophysical Research Letters*, *43*(21), 11,414–11,422.

doi: 10.1002/2016GL071279

- Collins, W. D., Rasch, P. J., Boville, B. A., Hack, J. J., McCaa, J. R., Williamson, D. L., et al. (2004). Description of the NCAR community atmosphere model (CAM 3.0). *NCAR Tech. Note NCAR/TN-464+ STR*, 226, 1326–1334.
- Collins, W. D., Rasch, P. J., Boville, B. A., Hack, J. J., McCaa, J. R., Williamson, D. L., et al. (2006). The formulation and atmospheric simulation of the Community Atmosphere Model version 3 (CAM3). *Journal of Climate*, 19(11), 2144–2161. doi: 10.1175/JCLI3760.1
- Dütsch, H. (1978). Vertical ozone distribution on a global scale. *Pure and Applied Geophysics*, 116(2), 511–529. doi: 10.1007/BF01636904
- Eager, J. K., Reichelt, D. J., Mayne, N. J., Lambert, F. H., Sergeev, D. E., Ridgway, R. J., ... Kohary, K. (2020). Implications of different stellar spectra for the climate of tidally locked earth-like exoplanets. *Astronomy & Astrophysics*, 639, A99.
- Goldblatt, C. (2016). Comment on “Long-term climate forcing by atmospheric oxygen concentrations”. *Science*, 353(6295), 132–132.
- Goldblatt, C., Claire, M. W., Lenton, T. M., Matthews, A. J., Watson, A. J., & Zahnle, K. J. (2009). Nitrogen-enhanced greenhouse warming on early Earth. *Nature Geoscience*, 2(12), 891–896. doi: 10.1038/ngeo692
- Goldblatt, C., Robinson, T. D., Zahnle, K. J., & Crisp, D. (2013). Low simulated radiation limit for runaway greenhouse climates. *Nature Geoscience*, 6(8), 661–667. doi: 10.1038/ngeo1892
- Guendelman, I., & Kaspi, Y. (2019). Atmospheric dynamics on terrestrial planets: The seasonal response to changes in orbital, rotational, and radiative timescales. *The Astrophysical Journal*, 881(1), 67. doi: 10.3847/1538-4357/ab2a06
- Hartmann, D. L. (2015). *Global physical climatology* (Vol. 103). Elsevier.
- Holland, H. D. (2006). The oxygenation of the atmosphere and oceans. *Philosophical Transactions of the Royal Society B: Biological Sciences*, 361(1470), 903–915. doi: 10.1098/rstb.2006.1838
- Holton, J. R., & Hakim, G. J. (2013). *An introduction to dynamic meteorology (fifth edition)*. Academic Press. doi: 10.1016/B978-0-12-384866-6.00025-8
- Huang, R. X. (1993). Real freshwater flux as a natural boundary condition for the salinity balance and thermohaline circulation forced by evaporation and precipitation. *Journal of Physical Oceanography*, 23(11), 2428–2446. doi: 10.1175/1520-0485(1993)023<2428:RFFAAN>2.0.CO;2
- Jeevanjee, N., & Romps, D. M. (2018). Mean precipitation change from a deepening troposphere. *Proceedings of the National Academy of Sciences*, 115(45), 11465–11470.
- Johnson, B., & Goldblatt, C. (2015). The nitrogen budget of Earth. *Earth-Science Reviews*, 148, 150–173. doi: 10.1016/j.earscirev.2015.05.006
- Kaspi, Y., & Showman, A. P. (2015). Atmospheric dynamics of terrestrial exoplanets over a wide range of orbital and atmospheric parameters. *The Astrophysical Journal*, 804(1), 60. doi: 10.1088/0004-637X/804/1/60
- Keles, E., Grenfell, J. L., Godolt, M., Stracke, B., & Rauer, H. (2018). The effect of varying atmospheric pressure upon habitability and biosignatures of Earth-like planets. *Astrobiology*, 18(2), 116–132. doi: 10.1089/ast.2016.1632
- Khairoutdinov, M. F., & Randall, D. A. (2003). Cloud resolving modeling of the ARM summer 1997 IOP: Model formulation, results, uncertainties, and sensitivities. *Journal of Atmospheric Sciences*, 60(4), 607–625. doi: 10.1175/1520-0469(2003)060<0607:CRMOTA>2.0.CO;2
- Kilic, C., Raible, C. C., Stocker, T. F., & Kirk, E. (2017). Impact of variations of gravitational acceleration on the general circulation of the planetary atmosphere. *Planetary and space science*, 135, 1–16. doi: 10.1016/j.pss.2016.11.001
- Koll, D. D. B., & Cronin, T. W. (2018). Earth’s outgoing longwave radiation linear due to H<sub>2</sub>O greenhouse effect. *Proceedings of the National Academy of Sciences*, 115(41), 10293–10298. doi: 10.1073/pnas.1809868115
- Komacek, T. D., & Abbot, D. S. (2019). The atmospheric circulation and climate of

- terrestrial planets orbiting Sun-like and M Dwarf stars over a broad range of planetary parameters. *The Astrophysical Journal*, *871*(2), 245. doi: 10.3847/1538-4357/aafb33
- Kopparapu, R. K., Ramirez, R. M., SchottelKotte, J., Kasting, J. F., Domagal-Goldman, S., & Eymet, V. (2014). Habitable zones around main-sequence stars: Dependence on planetary mass. *The Astrophysical Journal Letters*, *787*(2), L29. doi: 10.1088/2041-8205/787/2/L29
- Kopparapu, R. K., Wolf, E. T., Arney, G., Batalha, N. E., Haqq-Misra, J., Grimm, S. L., & Heng, K. (2017). Habitable moist atmospheres on terrestrial planets near the inner edge of the habitable zone around M dwarfs. *The Astrophysical Journal*, *845*(1), 5. doi: 10.3847/1538-4357/aa7cf9
- Kopparapu, R. K., Wolf, E. T., Haqq-Misra, J., Yang, J., Kasting, J. F., Meadows, V., . . . Mahadevan, S. (2016). The inner edge of the habitable zone for synchronously rotating planets around low-mass stars using general circulation models. *The Astrophysical Journal*, *819*(1), 84. doi: 10.3847/0004-637X/819/1/84
- Lacis, A. A., & Oinas, V. (1991). A description of the correlated- $k$  distribution method for modeling nongray gaseous absorption, thermal emission, and multiple scattering in vertically inhomogeneous atmospheres. *Journal of Geophysical Research: Atmospheres*, *96*(D5), 9027–9063. doi: 10.1029/90JD01945
- Lambert, F. H., & Webb, M. J. (2008). Dependency of global mean precipitation on surface temperature. *Geophysical Research Letters*, *35*(16). doi: 10.1029/2008GL034838
- Lammer, H., & Bauer, S. (1991). Nonthermal atmospheric escape from Mars and Titan. *Journal of Geophysical Research: Space Physics*, *96*(A2), 1819–1825. doi: 10.1029/90JA01676
- Le Hir, G., Teitler, Y., Fluteau, F., Donnadieu, Y., & Philippot, P. (2014). The faint young Sun problem revisited with a 3-D climate–carbon model—Part 1. *Climate of the Past*, *10*(2), 697–713. doi: 10.5194/cp-10-697-2014
- Li, Z., Ide, K., Treut, H. L., & Ghil, M. (1997). Atmospheric radiative equilibria in a simple column model. *Climate dynamics*, *13*(6), 429–440. doi: 10.1007/s003820050175
- Lotsch, A., Friedl, M. A., Anderson, B. T., & Tucker, C. J. (2003). Coupled vegetation-precipitation variability observed from satellite and climate records. *Geophysical Research Letters*, *30*(14). doi: 10.1029/2003GL017506
- Madhusudhan, N. (2019). Exoplanetary atmospheres: Key insights, challenges, and prospects. *Annual Review of Astronomy and Astrophysics*, *57*, 617–663. doi: 10.1146/annurev-astro-081817-051846
- Mallik, C., Tomsche, L., Bourtsoukidis, E., Crowley, J. N., Derstroff, B., Fischer, H., et al. (2018). Oxidation processes in the eastern Mediterranean atmosphere: evidence from the modelling of HO<sub>x</sub> measurements over Cyprus. *Atmospheric Chemistry and Physics*, *18*(14), 10825–10847. doi: 10.5194/acp-18-10825-2018
- Marty, B., Zimmermann, L., Pujol, M., Burgess, R., & Philippot, P. (2013). Nitrogen isotopic composition and density of the Archean atmosphere. *Science*, *342*(6154), 101–104. doi: 10.1126/science.1240971
- Medeiros, B., Stevens, B., Held, I. M., Zhao, M., Williamson, D. L., Olson, J. G., & Bretherton, C. S. (2008). Aquaplanets, climate sensitivity, and low clouds. *Journal of Climate*, *21*(19), 4974–4991.
- Mlawer, E. J., Taubman, S. J., Brown, P. D., Iacono, M. J., & Clough, S. A. (1997). Radiative transfer for inhomogeneous atmospheres: RRTM, a validated correlated- $k$  model for the longwave. *Journal of Geophysical Research: Atmospheres*, *102*(D14), 16663–16682. doi: 10.1029/97JD00237
- Nagy, K. L. (2018). Dissolution and precipitation kinetics of sheet silicates. *Chemical Weathering Rates of Silicate Minerals*, 173–234. doi: 10.1515/9781501509650-007
- Nakajima, S., Hayashi, Y.-Y., & Abe, Y. (1992). A study on the “runaway greenhouse effect” with a one-dimensional radiative–convective equilibrium model. *Journal of Atmospheric Sciences*, *49*(23), 2256–2266. doi: 10.1175/1520-0469(1992)049<2256:ASOTGE>2.0.CO;2
- Neale, R. B., & Hoskins, B. J. (2000). A standard test for agcms including their physical

- parametrizations: I: The proposal. *Atmospheric Science Letters*, *1*(2), 101–107.
- Niemann, H. B., Atreya, S. K., Bauer, S. J., Carignan, G. R., Demick, J. E., Frost, R. L., et al. (2005). The abundances of constituents of Titan’s atmosphere from the GCMS instrument on the Huygens probe. *Nature*, *438*(7069), 779–784. doi: 10.1038/nature04122
- O’Gorman, P. A., Allan, R. P., Byrne, M. P., & Previdi, M. (2012). Energetic constraints on precipitation under climate change. *Surveys in geophysics*, *33*(3), 585–608. doi: 10.1007/s10712-011-9159-6
- Paradise, A., Fan, B. L., Menou, K., & Lee, C. (2021). Climate diversity in the solar-like habitable zone due to varying background gas pressure. *Icarus*, *358*, 114301. doi: 10.1016/j.icarus.2020.114301
- Paynter, D., & Ramaswamy, V. (2011). An assessment of recent water vapor continuum measurements upon longwave and shortwave radiative transfer. *Journal of Geophysical Research: Atmospheres*, *116*(D20). doi: 10.1029/2010JD015505
- Pendergrass, A. G., & Hartmann, D. L. (2014). The atmospheric energy constraint on global-mean precipitation change. *Journal of climate*, *27*(2), 757–768. doi: 10.1175/JCLI-D-13-00163.1
- Pierrehumbert, R. T. (2002). The hydrologic cycle in deep-time climate problems. *Nature*, *419*(6903), 191–198. doi: 10.1038/nature01088
- Pierrehumbert, R. T. (2010). *Principles of planetary climate*. Cambridge University Press. doi: 10.1017/CBO9780511780783
- Poulsen, C. J., Tabor, C., & White, J. D. (2015). Long-term climate forcing by atmospheric oxygen concentrations. *Science*, *348*(6240), 1238–1241. doi: 10.1126/science.1260670
- Ramanathan, V., & Downey, P. (1986). A nonisothermal emissivity and absorptivity formulation for water vapor. *Journal of Geophysical Research: Atmospheres*, *91*(D8), 8649–8666. doi: 10.1029/JD091iD08p08649
- Shields, A. L., Bitz, C. M., & Palubski, I. (2019). Energy budgets for terrestrial extrasolar planets. *The Astrophysical Journal Letters*, *884*(1), L2. doi: 10.3847/2041-8213/ab44ce
- Showman, A. P., Wordsworth, R. D., Merlis, T. M., & Kaspi, Y. (2013). Atmospheric circulation of terrestrial exoplanets. *Comparative Climatology of Terrestrial Planets*, *1*, 277–326.
- Som, S. M., Buick, R., Hagadorn, J. W., Blake, T. S., Perreault, J. M., Harnmeijer, J. P., & Catling, D. C. (2016). Earth’s air pressure 2.7 billion years ago constrained to less than half of modern levels. *Nat. Geosci.*, *9*(6), 448. doi: doi.org/10.1038/ngeo2713
- Thomson, S. I., & Vallis, G. K. (2019). The effects of gravity on the climate and circulation of a terrestrial planet. *Quarterly Journal of the Royal Meteorological Society*, *145*(723), 2627–2640.
- Trenberth, K. E., & Shea, D. J. (2005). Relationships between precipitation and surface temperature. *Geophysical Research Letters*, *32*(14). doi: 10.1029/2005GL022760
- Turbet, M., Bolmont, E., Leconte, J., Forget, F., Selsis, F., Tobie, G., . . . Gillon, M. (2018). Modeling climate diversity, tidal dynamics and the fate of volatiles on TRAPPIST-1 planets. *Astronomy & Astrophysics*, *612*, A86. doi: 10.1051/0004-6361/201731620
- Vallis, G. K. (2017). *Atmospheric and oceanic fluid dynamics*. Cambridge University Press.
- Walker, J. C. G., Hays, P., & Kasting, J. F. (1981). A negative feedback mechanism for the long-term stabilization of Earth’s surface temperature. *Journal of Geophysical Research: Oceans*, *86*(C10), 9776–9782. doi: 10.1029/JC086iC10p09776
- Wolf, E. T., Kopparapu, R., Haqq-Misra, J., & Faucher, T. J. (2022). Exocam: A 3d climate model for exoplanet atmospheres. *The Planetary Science Journal*, *3*(1), 7. doi: 10.3847/PSJ/ac3f3d
- Wolf, E. T., Shields, A. L., Kopparapu, R. K., Haqq-Misra, J., & Toon, O. B. (2017). Constraints on climate and habitability for Earth-like exoplanets determined from a general circulation model. *The Astrophysical Journal*, *837*(2), 107. doi: 10.3847/1538-4357/aa5ffc



- Wolf, E. T., & Toon, O. B. (2013). Hospitable Archean climates simulated by a general circulation model. *Astrobiology*, *13*(7), 656–673. doi: 10.1089/ast.2012.0936
- Wolf, E. T., & Toon, O. B. (2014). Controls on the Archean climate system investigated with a global climate model. *Astrobiology*, *14*(3), 241–253. doi: 10.1089/ast.2013.1112
- Wolf, E. T., & Toon, O. B. (2015). The evolution of habitable climates under the brightening Sun. *Journal of Geophysical Research: Atmospheres*, *120*(12), 5775–5794. doi: 10.1002/2015JD023302
- Xiong, J., & Yang, J. (2020). Examining the role of varying surface pressure in the climate of early Earth. *Climate of the Past Discussions*, 1–20. doi: 10.5194/cp-2020-55
- Xiong, J., Yang, J., & Nie, J. (2020). Possible dependence of climate on atmospheric mass: A convection–circulation–cloud coupled feedback. *Journal of the Atmospheric Sciences*, *77*(11), 3833–3846. doi: 10.1175/JAS-D-20-0022.1
- Yang, H., Komacek, T. D., & Abbot, D. S. (2019). Effects of radius and gravity on the inner edge of the habitable zone. *The Astrophysical Journal Letters*, *876*(2), L27. doi: 10.3847/2041-8213/ab1d60
- Yang, H., & Yang, J. (2019). How do planetary radius and gravity influence the surface climate of earth-like planets? *arXiv:1910.06479*.
- Yang, J., Cowan, N. B., & Abbot, D. S. (2013). Stabilizing cloud feedback dramatically expands the habitable zone of tidally locked planets. *The Astrophysical Journal Letters*, *771*(2), L45.
- Yang, J., Leconte, J., Wolf, E. T., Goldblatt, C., Feldl, N., Merlis, T., . . . others (2016). Differences in water vapor radiative transfer among 1D models can significantly affect the inner edge of the habitable zone. *The Astrophysical Journal*, *826*(2), 222. doi: 10.3847/0004-637X/826/2/222
- Yang, J., Peltier, W. R., & Hu, Y. (2016). Monotonic decrease of the zonal SST gradient of the equatorial Pacific as a function of CO<sub>2</sub> concentration in CCSM3 and CCSM4. *Journal of Geophysical Research: Atmospheres*, *121*(18), 10–637. doi: 10.1002/2016JD025231
- Zhang, G. J., & McFarlane, N. A. (1995). Sensitivity of climate simulations to the parameterization of cumulus convection in the Canadian Climate Centre general circulation model. *Atmosphere-Ocean*, *33*(3), 407–446. doi: 10.1080/07055900.1995.9649539
- Zhang, Y., Jeevanjee, N., & Fueglistaler, S. (2020). Linearity of outgoing longwave radiation: From an atmospheric column to global climate models. *Geophysical Research Letters*, *47*(17), e2020GL089235. doi: 10.1029/2020GL089235
- Zhang, Y., & Yang, J. (2020). How does background air pressure influence the inner edge of the habitable zone for tidally locked planets in a 3D view? *The Astrophysical Journal Letters*, *901*(2), L36. doi: 10.3847/2041-8213/abb87f